LOW-TEMPERATURE HYDROTHERMAL ALTERATION OF TRACHYBASALT AT CONICAL SEAMOUNT, PAPUA NEW GUINEA: FORMATION OF SMECTITE AND METASTABLE PRECURSOR PHASES

Giovanna Giorgetti[1],*, Thomas Monecke[2], Reinhard Kleeberg[3], and Mark D. Hannington[4]

[1] Dipartimento di Scienze della Terra, Università di Siena, Via Laterina 8, 53100 Siena, Italy
[2] Department of Geology and Geological Engineering, Colorado School of Mines, 1516 Illinois Street, Golden, CO, 80401, USA
[3] Institut für Mineralogie, TU Bergakademie Freiberg, Brennhausgasse 14, D-09596 Freiberg, Germany
[4] Department of Earth Sciences, University of Ottawa, Marion Hall, 140 Louis Pasteur, Ottawa, ON, K1N 6N5, Canada

Abstract—The conversion of volcanic glass to secondary alteration products is one of the most common mineralogical transformations during low-temperature hydrothermal alteration of submarine basalts. To better understand the mechanism and kinetics of this transformation, porphyritic and formerly glassy trachybasalt, recovered from Conical Seamount, Papua New Guinea, was studied in detail. Low-temperature interaction of trachybasalt with hydrothermal fluids at this submerged volcano occurred in response to the formation of submarine epithermal-style gold mineralization. Alteration of the coherent volcanic rocks is heterogeneous with pronounced differences in alteration intensity occurring between igneous minerals and the surrounding glassy groundmass. In comparison to the volcanic glass, the crystalline phases were less prone to hydrothermal alteration with the alteration susceptibility decreasing from clinopyroxene through biotite to feldspar. Low-temperature alteration of clinopyroxene resulted in the formation of abundant saponite-like smectite with no topotactic relationship being observed between the two phases. In contrast, the conversion of biotite to smectite involved structural inheritance as the orientation of common structural blocks was maintained during alteration. Transmission and analytical electron microscopy revealed that pervasive alteration of interstitial glass in the groundmass of the trachybasalt resulted in the formation of montmorillonite- and saponite-like smectite whereby smectite composition is strongly influenced by the glass chemistry. The occurrence of poorly crystalline domains with a 0.3 to 0.4 nm layer spacing in the altered interstitial glass suggests that the transformation of glass to smectite involved the formation of a transitional alteration product. Comparison with the results of previous studies highlights the fact that the glass-to-smectite transformation can proceed through more than one reaction pathway. Reaction style and reaction progress are controlled by kinetic factors such as the mode of fluid transport triggering alteration in the low-temperature hydrothermal environment. Alteration of the trachybasalt at Conical Seamount is inferred to have taken place at a comparably low fluid-rock ratio as the low permeability and the absence of primary fractures and joints restricted fluid circulation through the coherent volcanic rocks.

Key Words—Conical Seamount, Hydrothermal Alteration, Glass-to-smectite Transition, Volcanic Glass, Metastable Precursors, Smectite, Transmission Electron Microscopy.

INTRODUCTION

Low-temperature alteration of seafloor basalts represents one of the principal controls on the geochemical budget of the oceans (Humphris and Thompson, 1978; Edmond *et al.*, 1979; Staudigel and Hart, 1983; Mottl and Wheat, 1994; Spivack and Staudigel 1994; Kadko *et al.*, 1995). The conversion of volcanic glass to secondary alteration products is the most important mineral transformation associated with this process (Staudigel and Hart, 1983) because glass contained in seafloor basalts is thermodynamically unstable and more susceptible to alteration than most associated primary minerals.

Previous investigations have shown that the low-temperature hydration and alteration of mafic volcanic glass results in the formation of smectite, with celadonite, zeolites, and carbonate minerals being other common devitrification products (Andrews, 1980; Alt *et al.*, 1986, 1998; Shau and Peacor, 1992; Li *et al.*, 1997; Marescotti *et al.*, 2000; Giorgetti *et al.*, 2001; Zhou *et al.*, 2001; Alt and Teagle, 2003). Alteration commonly proceeds through the formation of palagonite (Peacock, 1926), an extremely fine-grained mixture of amorphous to poorly crystalline phases (Stroncik and Schmincke, 2001).

Despite intense research, the mechanism and kinetics of palagonitization and the processes involved in the neoformation of thermodynamically stable alteration products such as smectite remain subjects of debate. Several studies have shown that palagonitization initially involves the formation of spheroidal protocrystallites that are subsequently replaced by smectite

(Eggleton and Keller, 1982; Zhou and Fyfe, 1989; Zhou *et al.*, 1992). However, such protocrystallites have not always been observed, suggesting that glass alteration can also occur by a process of dissolution and smectite precipitation with no intermediate alteration products being formed (Giorgetti *et al.*, 2001; Zhou *et al.*, 2001).

The present study focuses on the low-temperature hydrothermal alteration of glassy trachybasalt from Conical Seamount, Papua New Guinea (Herzig *et al.*, 1994, 1999; Petersen *et al.*, 2002). Volcanic rocks from this submarine volcanic complex show geochemical signatures characteristic of highly potassic igneous rocks occurring in oceanic island arc settings (Müller *et al.*, 2003). Results are presented here of a combined scanning electron microscopy (SEM), X-ray diffraction (XRD), transmission electron microscopy (TEM), and analytical electron microscopy (AEM) study that was carried out to characterize the products of low-temperature hydrothermal alteration of these volcanic rocks. Comparison with the results of previous investigations permits a new assessment of the mechanisms of low-temperature glass alteration and the factors controlling reaction pathway and reaction progress.

GEOLOGICAL SETTING

Conical Seamount is located in the New Ireland basin, Bismarck Archipelago, northeast of the main island of Papua New Guinea. The submarine volcano forms part of the Tabar-Lihir-Tanga-Feni volcanic chain that extends for ~260 km parallel to the coast of New Ireland (Figure 1). Silica-undersaturated alkaline volcanism along the island chain occurred in response to lithospheric extension along NE-trending faults cutting across the New Ireland basin, which were generated contemporaneously with the opening of the Manus back-arc basin (Stewart and Sandy, 1988; McInnes and Cameron, 1994). Subaerial volcanism commenced ~3.6 Ma ago at Simberi Island (Tabar Island group), with the most recent eruption on land being dated at Ambitle Island (Feni Island group) ~2300 y before present (Licence *et al.*, 1987; Rytuba *et al.*, 1993). The area is still seismically active and a number of shallow earthquake epicenters have been located near Lihir Island in recent decades (Herzig *et al.*, 1994; Petersen *et al.*, 2002).

Conical Seamount is located ~10 km to the south of Lihir Island. The submarine volcano has a basal diameter of ~2.8 km and forms a volcanic cone that rises to >600 m above the surrounding seafloor to a water depth of 1050 m (Herzig *et al.*, 1994; Petersen *et al.*, 2002). The upper part of the seamount comprises massive lava flows; individual flows appear to have cascaded down the steep flanks of the volcano producing small steps and terraces. Conical Seamount is characterized by a small summit plateau that is ~100 m by 200 m in size (Figure 1).

Detailed mapping and sampling carried out during three consecutive research cruises with the German research vessel (R/V) *Sonne* (Herzig *et al.*, 1994, 1999; Petersen *et al.*, 2002, 2005) revealed that large portions of the summit area of Conical Seamount are covered by trachybasalt that experienced hydrothermal alteration related to the formation of an unusual submarine sulfide occurrence that is considered to represent a modern seafloor analogue to epithermal precious metal deposits
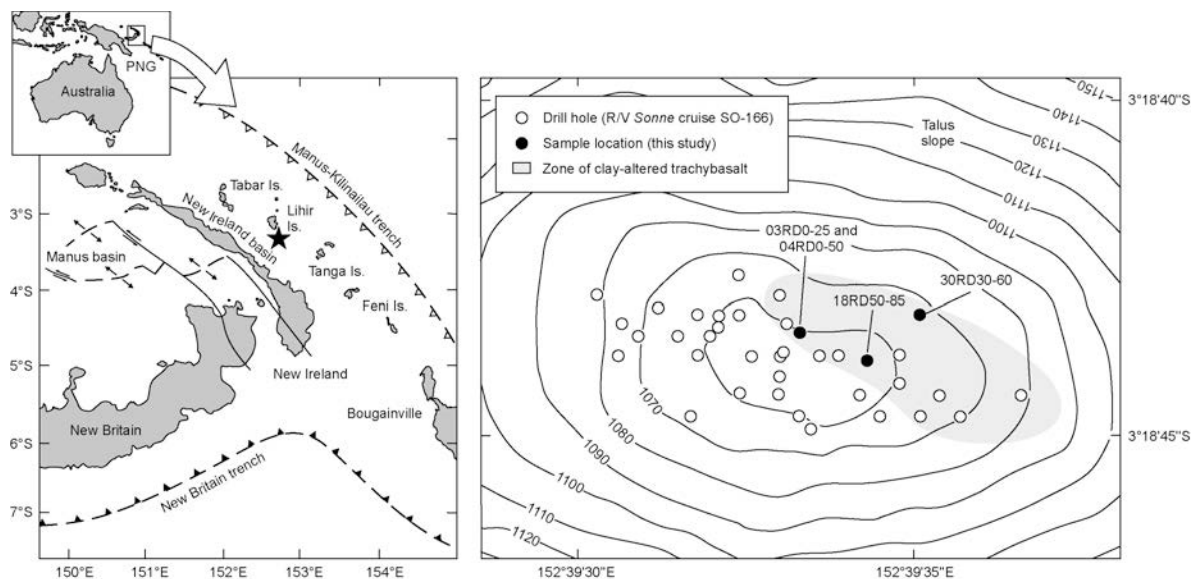

Figure 1. Regional map illustrating major tectonic elements in the New Ireland and Bismarck Sea region, and the location of Conical Seamount close to Lihir Island. The detailed map shows the summit plateau of the submerged volcano along with the sample locations (modified from Monecke *et al.*, 2003).

forming in volcanically active subaerial environments (Petersen *et al.*, 2002). At present, three distinct styles of mineralization have been recognized at Conical Seamount. Particularly widespread are stockwork-type veinlets and disseminations of marcasite and pyrite (Herzig *et al.*, 1999; Petersen *et al.*, 2002; Monecke *et al.*, 2003; Müller *et al.*, 2003; Gemmell *et al.*, 2004). In addition, polymetallic sulfide veins and breccia zones, consisting of amorphous silica, sphalerite, chalcopyrite, galena, pyrite, Cu-Pb-As-Sb sulfosalts, native gold, and electrum, have been locally observed (Herzig *et al.*, 1999; Petersen *et al.*, 2002; Monecke *et al.*, 2003). These veins and breccia zones are the main gold carrier at Conical Seamount, but are also typified by high concentrations of Ag, As, Sb, and Hg (Herzig *et al.*, 1999; Petersen *et al.*, 2002). A third style of mineralization comprises rare fracture linings and open space fillings of realgar, orpiment, stibnite, and minor pyrite (Herzig *et al.*, 1999; Petersen *et al.*, 2002).

SAMPLE SELECTION AND ANALYTICAL METHODS

Extensive sampling of the trachybasalt hosting the mineralization at Conical Seamount was conducted during R/V *Sonne* cruise SO-166 (Petersen *et al.*, 2005). A lander-type drilling device was used and successfully deployed to drill a large number of shallow holes in various areas of the summit plateau (Figure 1). Drilling was conducted to a maximum penetration depth of 5 m. The drill core obtained was logged on board to record the distribution of sulfide mineralization and variations in the relative abundance of alteration minerals.

To study the nature of hydrothermal alteration associated with the formation of the widespread stockwork-type veinlets and disseminations of marcasite and pyrite, over 30 drill core samples (25−60 cm long core intervals) were selected for mineralogical analysis. Initially, polished thin sections were prepared from all drill core samples and studied by optical microscopy and scanning electron microscopy. The SEM investigations were conducted on a JEOL JSM 6400 microscope, equipped with a Tracor (Noran) series II energy-dispersive X-ray (EDX) spectrometer. Routine operating conditions were 20 kV with a beam current of 600 pA, high-resolution back-scattered electron (BSE) images were collected at up to 4.5 nA.

Based on the detailed petrographic analysis of the thin sections and the SEM investigations, four representative clay-rich drill core samples (03RD0-25, 04RD0-50, 18RD50-85, and 30RD30-60) were selected for the present study. To study the mineralogy and geochemistry of the whole-rock samples, a quarter of the drill core samples was crushed to a grain size of <2 mm and washed repeatedly with distilled water and centrifuged. This procedure was employed to remove any seawater salt.

The preparation of samples for quantitative phase analysis by XRD using the Rietveld method required further crushing of a split of the salt-free, whole-rock material to a grain size of <0.4 mm. The finely crushed samples were split again and 1.80 g of sample material was subsequently mixed with 0.20 g of synthetic ZnO used as an internal standard. Fine grinding of the mixtures to a grain size of <10 μm was performed under ethanol in a McCrone micronizing mill for 8 min. After drying, the fine powders were homogenized in a vibratory mixer mill (precursor model to the mill Pulverisette 23, Fritsch GmbH, Idar-Oberstein, Germany).The powders were then filled into conventional top-loading holders. Step-scan XRD data were obtained using a URD-6 (Seifert-FPM) diffractometer that was equipped with a diffracted-beam graphite monochromator and a variable divergence slit. A Co tube was utilized and operated at 40 kV and 30 mA. Qualitative phase-analysis of the raw diffraction patterns was performed by a conventional search/match procedure. Subsequent quantitative phase analysis was performed using the method described by Monecke *et al.* (2003).

The clay mineralogy of the four samples was studied in further detail by XRD after separation of the <2 μm size fraction from the finely crushed (<0.4 mm) whole-rock samples. The clay-sized fractions were separated from the crushed material by standard methods of gravity sedimentation and centrifuging. Strongly oriented XRD samples were prepared from the clay-sized fractions obtained using the standard glass-slide method. Step-scan data (2−16º2θ, 0.05º2θ step width, 10 s/step) were collected on the strongly oriented samples after air-drying, ethylene glycol solvation, and heating at 550ºC for 2.4 h. In addition, random powder mounts of the clay-sized fractions were prepared and investigated by XRD using the measurement conditions described above.

Full-pattern fitting of the step-scan data collected on the random powder mounts was performed using the fundamental-parameter Rietveld program BGMN (Bergmann *et al.*, 1998) employing a single-layer approach developed by Ufer *et al.* (2004, 2008) to model the turbostratically disordered smectite structures. The automatic refinement included the optimization of scale factors, lattice parameters, some occupancy factors, and profile parameters for each phase as well as preferred orientation models for most phases present together with background, zero point, and sample displacement.

Sample preparation for the TEM and AEM investigations included the preparation of sticky-wax, polished thin sections of the four altered trachybasalt samples. Initially, Cu discs with a central aperture (600−800 μm diameter) were attached to the samples at texturally distinct sites (unaltered glassy groundmass, altered groundmass containing abundant clay minerals, and altered pyroxene phenocrysts). A total of nine mounted samples was subsequently removed and ion-milled using

a Gatan Dual Ion Mill 600. The TEM observations and AEM analyses were obtained using a JEOL 2010 microscope operated at 200 kV. The quantitative AEM analyses were carried out using an X-ray energy dispersive system (EDS) Link Isis EDX and a beam diameter of ~20 nm. The AEM spectra were processed using K-factors determined on natural ion-milled standards (paragonite, muscovite, albite, clinochlore, fayalite, rhodonite, and titanite).

RESULTS

Petrography and SEM investigations

The four samples investigated in the present study were recovered from coherent trachybasalt units covering the summit plateau of Conical Seamount (Figure 1). Optical microscopy revealed that the primary volcanic textures of the trachybasalt samples are, in general, well preserved despite the fact that the mineralogical composition of the samples has been substantially modified as a result of fluid-rock interaction. The lava is moderately vesicular (estimated 10 modal %) and highly porphyritic (estimated 20−25 modal %), with a phenocryst assemblage of clinopyroxene, plagioclase, and magnetite. The vesicles are typically small and rounded (<1 mm in diameter), but locally they are also elongate, almost tabular, and up to 10 mm long.

The clinopyroxene phenocrysts range up to 5 mm in size and are estimated to form 15−20 modal % of the samples. They occur as large euhedral and prismatic crystals that are evenly dispersed in a much finer-grained groundmass or form glomerophyric aggregates consisting of several intergrown, prismatic phenocrysts. The phenocrysts exhibit oscillatory growth zoning that is superposed on a well defined sector zoning. In addition to the clinopyroxene, ~5 modal % of the samples consist of lath-shaped plagioclase microphenocrysts that range from 0.3 to 0.5 mm in size. These microphenocrysts show lamellar growth twins and exhibit complex oscillatory zoning patterns. Magnetite microphenocrysts are also common in the samples investigated (estimated 1−4 modal %). The magnetite microphenocrysts are euhedral, but typically form clusters of two or more crystals having different sizes. The magnetite crystals are commonly embayed and contain inclusions of the formerly glassy groundmass. The magnetite microphenocrysts are frequently intergrown with the clinopyroxene phenocrysts, but also occur dispersed in the much finer-grained groundmass.

The groundmass of the trachybasalt samples is composed of interlocking, randomly oriented microlites that range from one to several tens of micrometers in size. Prismatic clinopyroxene microlites as well as lath-shaped plagioclase and sanidine microlites are common. Additional common microlites are small biotite platelets and euhedral magnetite crystals. Apatite represents a minor phase in the groundmass of all samples investi-

gated. The interstitial space between the microlites was originally occupied by volcanic glass.

Hydrothermal alteration of the trachybasalt samples most notably affected the large clinopyroxene phenocrysts (Figure 2a). Alteration is most pronounced at the outer margins of the phenocrysts where clay minerals, and locally marcasite or pyrite, replace the clinopyroxene to form replacement zones that are several tens to hundreds of micrometers thick (Figure 2b). In addition, replacement by clay minerals occurs along irregular transverse and longitudinal fractures as well as zones that parallel contacts of intergrown clinoproxene crystals forming glomerocrysts (Figure 2c). Preferential replacement of certain oscillatory growth zones and melt inclusions contained in the clinopyroxene phenocrysts is common. Advanced alteration of the clinopyroxene phenocrysts resulted in the formation of irregularly shaped residual cores that are set in a matrix consisting of clay minerals and minor sulfides.

In contrast to the clinopyroxene phenocrysts, the plagioclase microphenocrysts appear largely unaltered (Figure 2d). However, the magnetite microphenocrysts are commonly affected by intense hydrothermal alteration and are usually partly or entirely replaced by secondary minerals. Alteration typically proceeded from the margins of the grains inwards or along transverse fractures. Extensive replacement of magnetite by marcasite and pyrite is common, but locally the sulfides only form rims surrounding the former magnetite microphenocrysts whereas their interiors are replaced by chemically heterogeneous material (Figure 2e).

Hydrothermal alteration of the groundmass of the trachybasalt primarily affected the interstitial glass as well as the clinopyroxene microlites. Advanced alteration led to a pervasive replacement of the groundmass and the formation of small and commonly wavy clay aggregates and finely dispersed pyrite and marcasite. The plagioclase and sanidine microlites appear to be texturally unmodified and now form a framework that surrounds the secondary clay aggregates (Figure 2f). Analcime was locally observed in the formerly glassy groundmass of sample 30RD30-60. This zeolite group mineral appears to replace interstitial glass, but locally, also forms thin veinlets transecting phenocrysts and microphenocrysts.

X-ray diffraction on whole-rock samples

Rietveld analysis performed on the step-scan data collected on the whole-rock powders revealed that the hydrothermally altered trachybasalt contains between 15 and 30 wt.% diopside. In addition to diopside, the samples are typified by large plagioclase and sanidine contents, which together comprise 40−55 wt.% (Table 1).

Rietveld refinement showed that the contribution of plagioclase to the overall XRD patterns could be most accurately described using two structural models,

namely a bytownite and a triclinic K-poor high-albite starting structure. The composition of sanidine present in

the samples is also complex and required the use of two monoclinic high-sanidine starting structures having
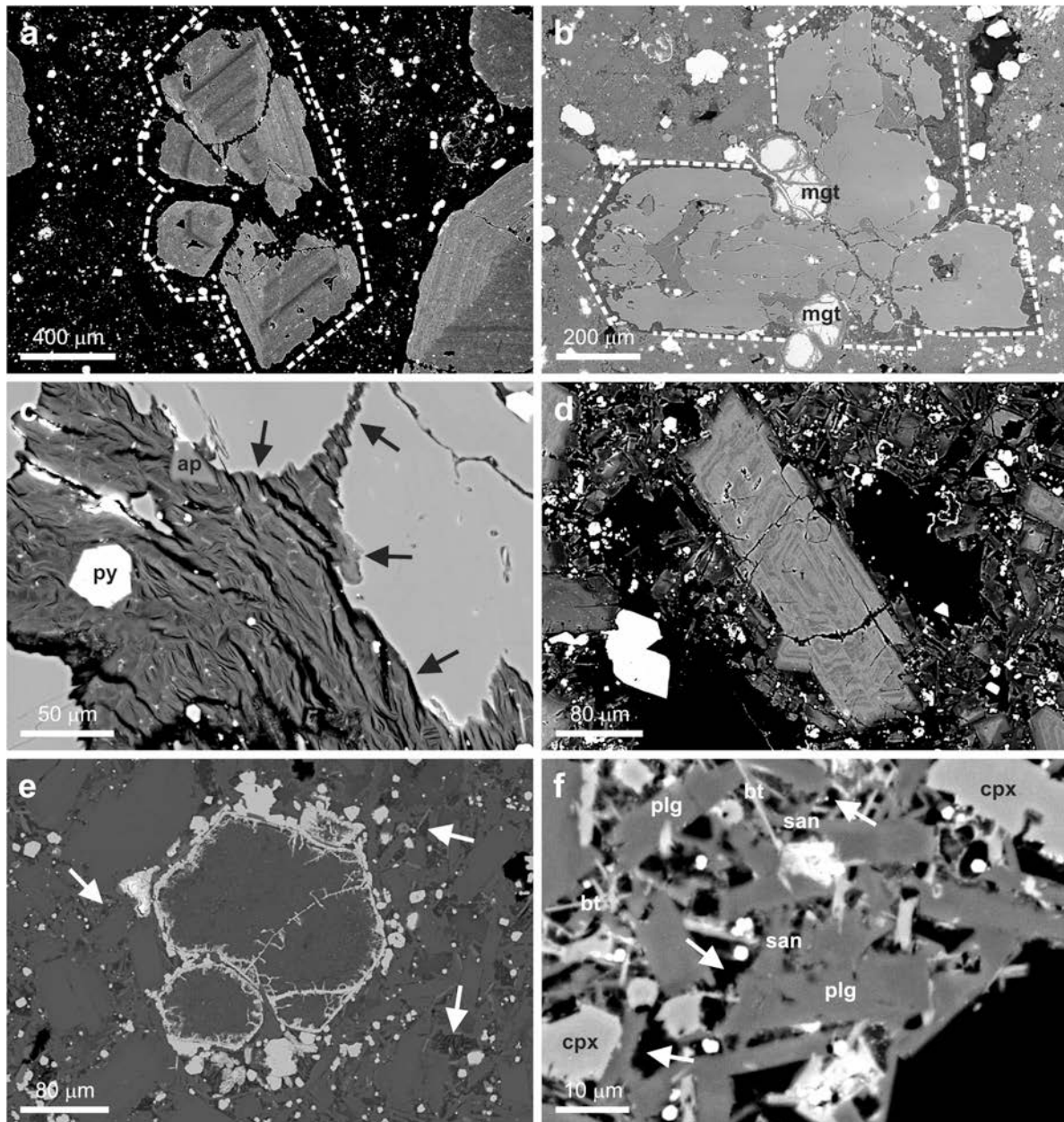

Figure 2. SEM images of altered trachybasalt: (a) BSE image of an altered pyroxene glomerocryst. Alteration is pronounced at the outer margins of the crystal aggregate (dotted line) and along contacts between intergrown crystals. (b) Secondary electron image of an altered pyroxene aggregate. Alteration proceeded preferentially along the contacts of intergrown pyroxene crystals and along the outer margins of the aggregate (dotted line). Primary magnetite (mgt) is partially replaced by fine-grained secondary alteration products. (c) BSE image of a pyroxene crystal that is partially replaced by smectite. The arrows indicate the replacement front. ap: primary apatite; py: secondary pyrite. (d) BSE image of a plagioclase phenocryst with complex compositional zoning. Replacement of the plagioclase by secondary minerals is not observed. The groundmass surrounding the crystal is intensely altered. (e) BSE image of an altered magnetite microphenocryst that is entirely replaced by fine-grained secondary alteration products. Secondary pyrite and marcasite mark the outline of the former microphenocryst. The surrounding groundmass is altered with interstitial glass being partially replaced by smectite (arrows). (f) BSE image of altered groundmass composed of interlocking microlites of plagioclase (plg), pyroxene (cpx), sanidine (san), and biotite (bt). Interstitial glass (arrows) is partially replaced by secondary smectite.

different Na-contents. Peak overlap was found to be substantial for the triclinic and monoclinic phases, respectively, hampering reliable quantification of the relative abundance of the four different feldspars. Therefore, only the totals calculated for the triclinic and monoclinic feldspars are listed in Table 1.

The altered trachybasalt samples contain between 5 and 8 wt.% biotite. Other primary components of the trachybasalt occur at distinctly lower abundances. Magnetite was only detected by XRD in samples 18RD50-85 and 30RD30-60. Sample 03RD0-25 was found to contain ~0.5 wt.% apatite (Table 1).

The XRD patterns collected on the altered samples were found to lack a broad amorphous scattering hump typical of unaltered volcanic rocks containing abundant volcanic glass. This observation suggests that the samples contain only moderate to small amounts of amorphous material, which is in agreement with the microscopic observations. Quantification of the amount of volcanic glass present was, however, precluded by the complex mineralogical nature of the samples. All four samples investigated contain abundant smectite showing turbostratic disorder and are typified by the presence of more than one smectite species (see below). Although recent developments now permit modeling of smectite showing turbostratic disorder by the Rietveld method (Ufer *et al.*, 2004, 2008), reliable quantification of more than one disordered smectite species in the presence of

amorphous material is currently not possible. Therefore, the internal standard was used to constrain the total amount of smectite and volcanic glass contained in the samples (Table 1). The results indicate that all four samples contain <20 wt.% smectite.

In addition to clay minerals, the altered trachybasalt samples contain abundant secondary sulfides. In total, 4−8 wt.% of the trachybasalt is composed of pyrite and marcasite. Trace amounts of anatase (<0.5 wt.%) were detected in sample 03RD0-25. Sample 30RD30-60 was found to contain a small amount of analcime (~1.0 wt.%), which corroborates the results of the microscopic investigations.

X-ray diffraction of clay-sized fraction

In addition to the whole-rock samples, the <2 μm fractions of the four altered trachybasalt samples were investigated by XRD to study the products of hydrothermal alteration in more detail.

These investigations revealed that the low-2θ regions of the diffraction patterns collected on air-dried, strongly oriented samples are dominated by a broad reflection at 12.5−16.5 Å (Figure 3). In ethylene glycol-solvated conditions, the position of this peak increased to 16.8−17.0 Å (second order reflection at 8.4−8.5 Å) whereas heating at 550ºC resulted in a shift to 9.6 Å. Such behavior is characteristic of smectite whereby the broad first-order peak is caused by non-uniform basal

Table 1. Mineralogical composition (wt.%) of hydrothermally altered trachybasalt from Conical Seamount. Quantitative phase analysis was performed by XRD using the Rietveld method.

	03RD0-25	04RD0-50	18RD50-85	30RD30-60
Quantitative phase analysis				
Analcime	−	−	−	1.0±0.4
Anatase	0.3±0.2	−	−	−
Apatite	0.6±0.2	−	−	−
Biotite	8.4±0.9	7.0±0.7	6.8±0.7	5.4±0.8
Diopside	14.6±0.8	23.4±0.9	18.7±0.9	27.8±1.1
Marcasite	1.5±0.3	2.0±0.2	1.6±0.3	−
Magnetite	−	−	2.3±0.5	4.0±0.6
Plagioclase	32.5±4.4	35.7±4.7	29.1±4.5	22.3±2.8
Pyrite	6.5±0.3	3.8±0.2	4.7±0.2	4.1±0.3
Sanidine	18.1±1.8	21.0±2.8	18.9±3.7	19.3±5.9
Clay minerals/volcanic glass	17.5±5.3	7.1±6.4	17.9±4.9	16.1±2.8
R_{wp} %	5.60	4.76	5.09	6.02
R_{exp} %	3.48	3.56	3.55	3.55
S	1.61	1.34	1.43	1.70
Qualitative phase analysis				
Kaolinite	n.d.	n.d.	n.d.	present
Di-smectite	present	present	present	present
Tri-smectite	present	present	present	present
Vermiculite	present	present	present	n.d.

n.d. = not detected or not present
R_{wp} = weighted residual error
R_{exp} = expected error
S = goodness of fit

spacings, presumably due to the presence of variable amounts of interlayer water and/or variations in the interlayer cation occupancy. In addition to the basal reflection of smectite, the air-dried samples show a sharp reflection at 10.1 Å that is not influenced by ethylene glycol treatment. The peak, interpreted to be the 001 reflection of biotite, increased in intensity upon heating (Figure 3). In some samples, the peak also shifted
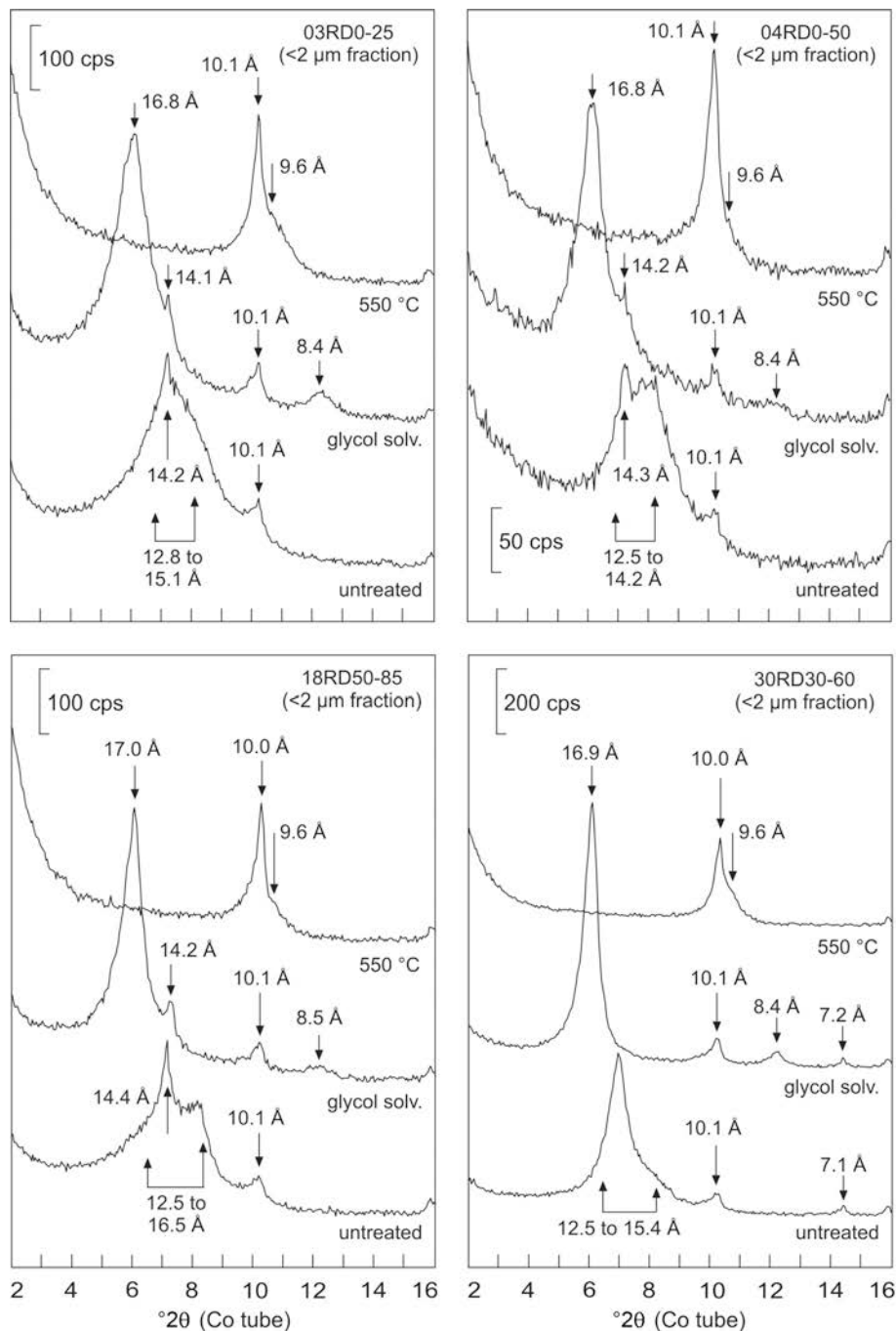
Figure 3. XRD patterns (strongly oriented mounts) collected from the <2 μm fractions of the hydrothermally altered trachybasalt samples. Substantial amounts of smectite (basal reflections: untreated = 12.5−16.5 Å, ethylene glycol-solvated = 16.8−17.0 Å and 8.4−8.5 Å, heated to 550ºC = 9.6 Å) are present. In addition, vermiculite (basal reflections: untreated and ethylene glycol-solvated = 14.1−14.4 Å, heated to 550ºC = 10.1 Å) is observed in samples 03RD0-25, 04RD0-50, and 18RD50-85. Traces of kaolinite occur in sample 30RD30-60 (basal reflection: untreated and ethylene glycol-solvated = 7.1−7.2 Å, not observed after heating to 550ºC).

slightly toward smaller *d* values in response to heating at 550ºC suggesting that the biotite may contain some interlayer water molecules.

The XRD patterns obtained from three of the four air-dried, strongly oriented samples (03RD0-25, 04RD0-50, and 18RD50-85) contain an additional sharp peak centered at 14.2 Å. The peak is not affected by the ethylene glycol treatment, but shifts to ~10 Å in response to heating (Figure 3) suggesting that this Bragg reflection represents the first basal reflection of vermiculite. The higher-order basal reflections of vermiculite are presumably not noticeable in the diffraction patterns of the air-dried samples because they possess significantly smaller relative intensities. Sample 30RD30-60 contains traces of kaolinite as demonstrated by a sharp peak at 7.15 Å which disappears upon heating (Figure 3).

Following investigations of the strongly oriented samples, the clay-sized fractions of the four altered trachybasalt samples were used to prepare random powder mounts. The 69−77º2θ region of the XRD patterns collected on the samples prepared in this way show a complex overlap of reflections (Figure 4). The region is dominated by a broad reflection at 1.49−1.50 Å, the position and shape of which suggests that this broad peak represents the 06,33 reflection of dioctahedral smectite. In addition, a sharp and intense peak can be observed at 1.54 Å which represents the 060 reflection of biotite. However, the asymmetric shape of the peak suggests that the sharp 060 biotite reflection

overlaps with the reflection of an additional phase. Profile fitting revealed that this reflection is located at ~1.53 Å suggesting the presence of a trioctahedral smectite, probably saponite. The relative abundance of this phase varies between the samples and is lowest in the trachybasalt 18RD50-85 (Figure 4).

The occurrence of trioctahedral smectite in addition to biotite and a dioctahedral smectite species is also confirmed by the occurrence of corresponding lower-order reflections in the 21−25º2θ region of the XRD patterns collected on the random powder mounts. This part of the diffraction patterns is dominated by the broad 02,11 asymmetric band of the dioctahedral smectite at 4.45 to 4.46 Å. In samples containing relatively large amounts of trioctahedral smectite, an additional shoulder can be observed at 4.59 Å. Overlap with the 020 reflection of biotite at ~4.62 Å is typically pronounced (Figure 5).

TEM observations and AEM analyses

Transmission and analytical electron microscopy were performed on representative ion-milled mounts. In general, the textural relationships observed at the nanoscale were similar for all trachybasalt samples investigated.

Low-magnification TEM imaging of the groundmass of the altered trachybasalt revealed the presence of abundant smectite crystals replacing volcanic glass (Figure 6). The bent smectite flakes are up to 70 nm thick, highly defective, and show random orientations. In
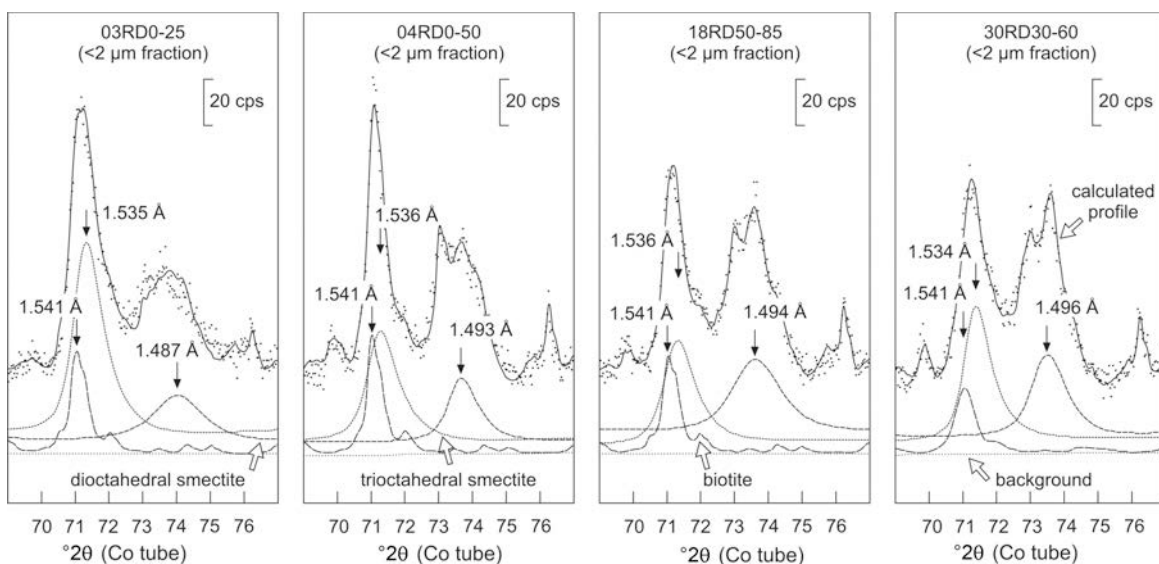

Figure 4. XRD patterns (random powder mounts, 69−77º2θ region) of the <2 μm fractions of the hydrothermally altered trachybasalt samples. Full-pattern fitting (points = measured data, solid line = fitted XRD profile) of the step-scan data was performed by the Rietveld method. The fitted profiles of dioctahedral and trioctahedral smectite as well as biotite are shown to illustrate the contributions of these phases to the overall diffraction profile, but all other phases were omitted for clarity. Note that the position and shape of the broad reflection centered at 1.54 Å cannot be described accurately without assuming the presence of trioctahedral smectite.
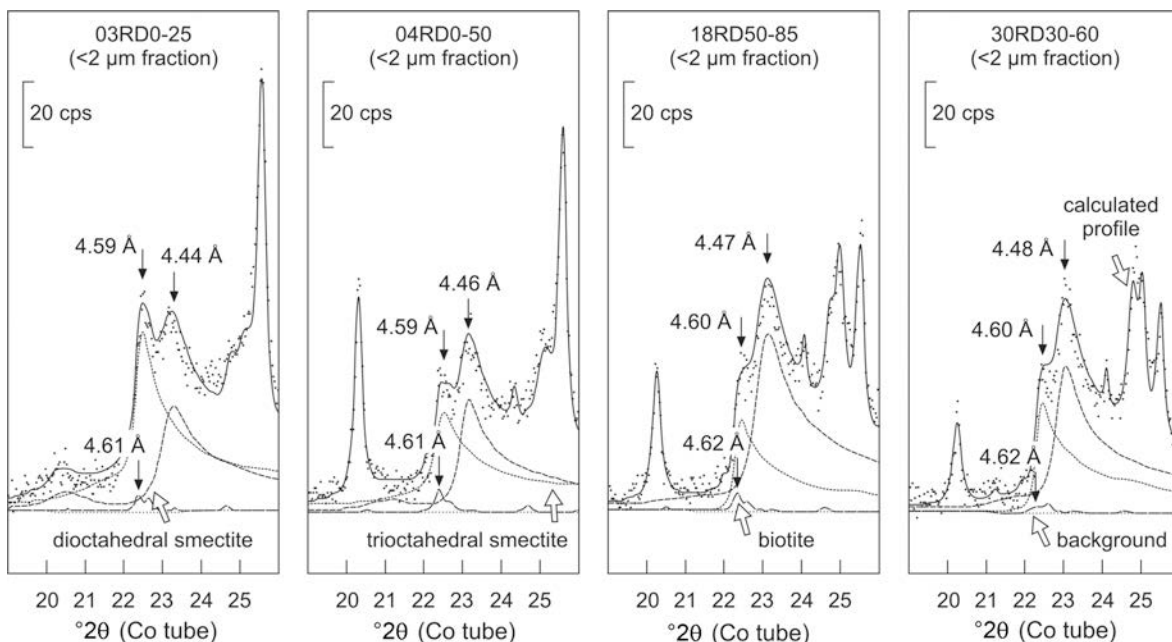
Figure 5. XRD patterns (random powder mounts, 19−26°2θ region) of the <2 μm fractions of the hydrothermally altered trachybasalt samples. Full-pattern fitting (points = measured data, solid line = fitted XRD profile) of the step-scan data has been performed by the Rietveld method. The fitted profiles of dioctahedral and trioctahedral smectite as well as biotite are shown to demonstrate the contributions of these phases to the overall diffraction profile. The fitted profiles of all other phases were omitted for clarity. Note that the broad 02,11 asymmetric band of the dioctahedral smectite at 4.45-4.46 Å has a shoulder at 4.59 Å that cannot be described accurately without assuming the presence of trioctahedral smectite.

addition to smectite, irregularly shaped or elongated domains characterized by up to 20 lattice fringes with a spacing of 0.3 to 0.4 nm were observed in the formerly glassy groundmass of the four samples investigated (Figure 7a,b). These irregularly shaped domains only occur in close spatial association with smectite flakes and are interpreted to represent transitional alteration phases forming during the glass-to-smectite transformation. Chemical analysis of these domain structures could not be obtained due to their small sizes.

Contacts between smectite and feldspars are always sharp at the nanoscale and no structural relationship was observed between the two phases (Figure 8a,b). The SEM imaging of feldspar crystals occurring in the altered groundmass (Figure 2d) suggests that the randomly oriented smectite flakes rimming feldspar crystals probably formed largely at the expense of former interstitial glass surrounding the crystals rather than by alteration of the feldspar crystals themselves.

In contrast to feldspar, primary clinopyroxene and biotite contained in the altered trachybasalt samples are partially replaced by smectite. Clinopyroxene crystals and secondary smectite flakes show no structural continuity across contacts suggesting that the crystallographic orientation of clinopyroxene is not inherited by the alteration product (Figure 9). In contrast to pyroxene, replacement of biotite by smectite appears to have involved inheritance of structural blocks from the

precursor to the alteration product. The basal planes of smectite replacing biotite are parallel to those of the trioctahedral mica (Figure 10) indicating that the orien-
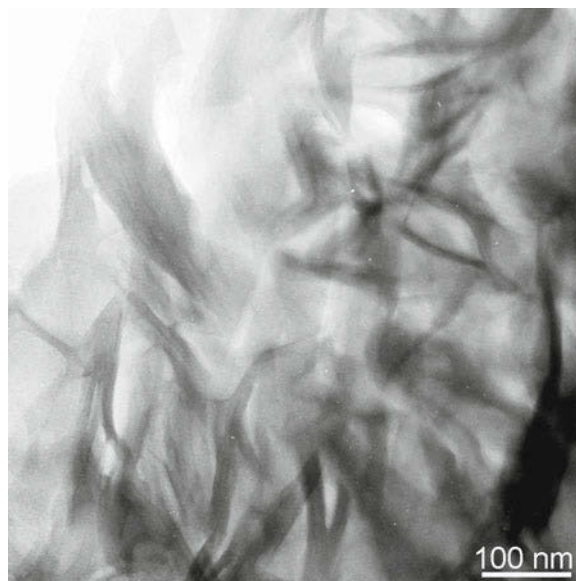

Figure 6. Low-magnification TEM image of smectite flakes formed by replacement of interstitial glass. The flakes are randomly oriented, bent, and up to 70 nm thick.
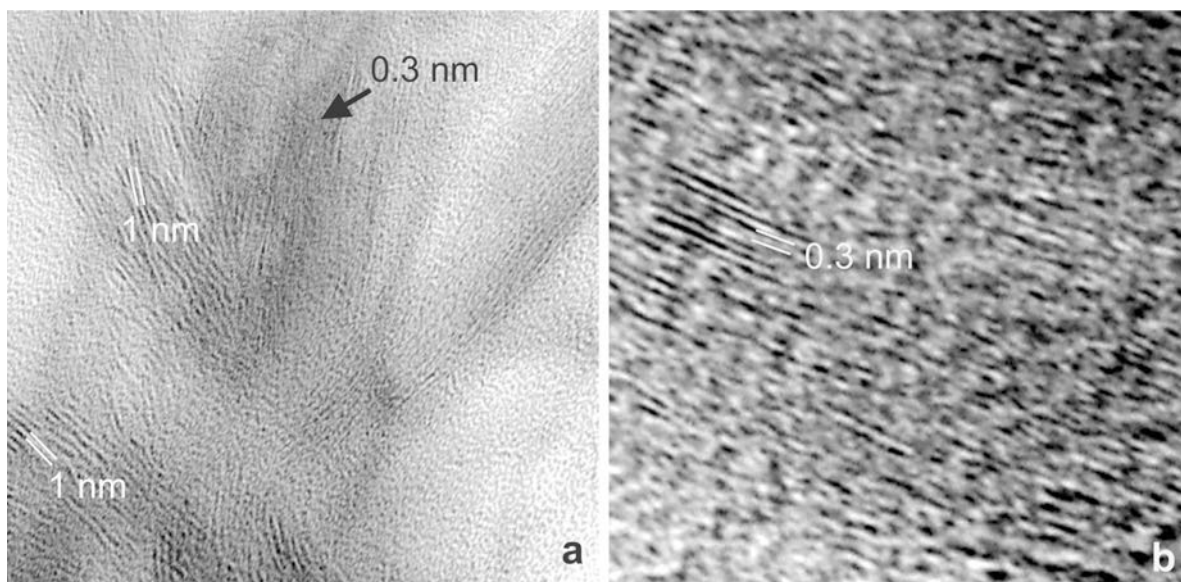
Figure 7. TEM images showing 0.3 to 0.4 nm domain structures that are interpreted to represent transitional alteration products forming during low-temperature glass alteration: (a) low-magnification image showing domains with 0.3−0.4 nm-spaced lattice fringes that occur in close association with defective and wavy smectite flakes having 1 nm lattice fringes. (b) High-resolution image of 0.3−0.4 nm-spaced fringes.

tation of structural building blocks is maintained during biotite alteration.

The chemical compositions of representative smectite flakes are reported in Tables 2 and 3. Analysis by AEM revealed that smectite replacing interstitial glass (Table 2) spans a broad range of compositions, with systematic differences being present between the four samples investigated. Smectite analyzed in samples 04RD0-50 and 18RD50-85 is typically dioctahedral, with octahedral Al concentrations ranging from 2.57 to 3.38 atoms per
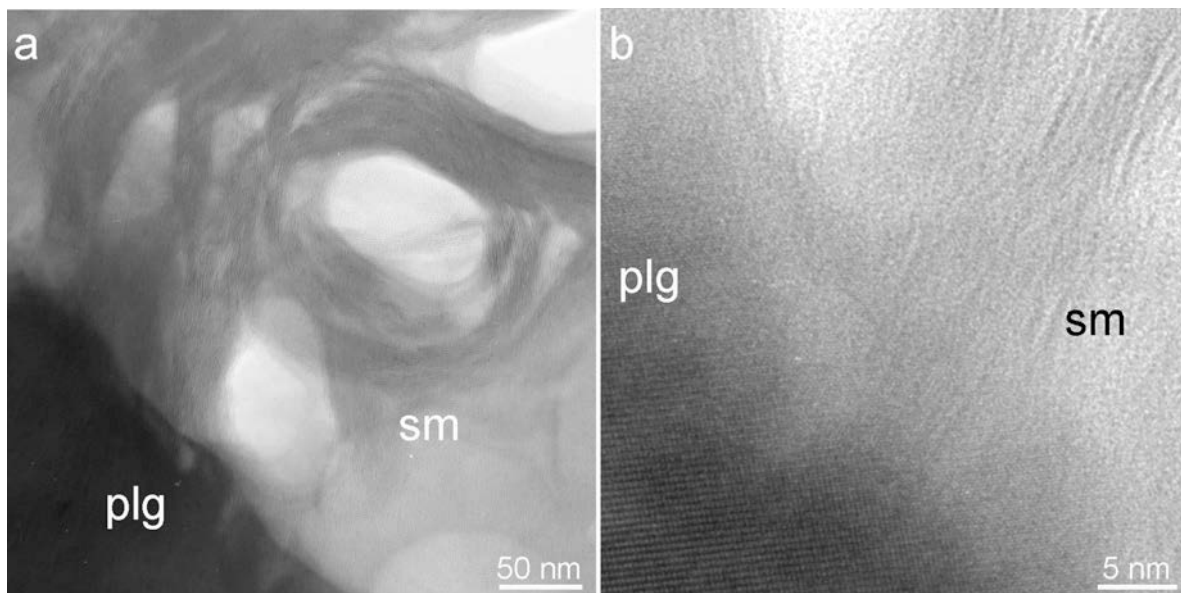

Figure 8. TEM images illustrating textural relationships between smectite and plagioclase: (a) low-magnification image showing a plagioclase crystal (plg) that is rimmed by randomly oriented smectite flakes (sm). (b) The lattice fringes of plagioclase and smectite are visible in this enlargement of the contact between the two phases. No structural relationship exists between the plagioclase and the smectite flakes. The smectite is interpreted to have formed as an alteration product of interstitial glass surrounding the plagioclase.
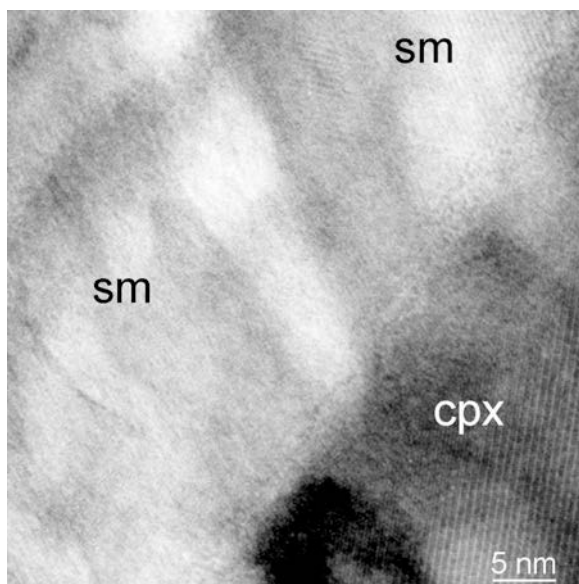
Figure 9. TEM image of an altered pyroxene crystal (cpx) that is partially replaced by smectite (sm). No structural relationship is observed between the two phases.
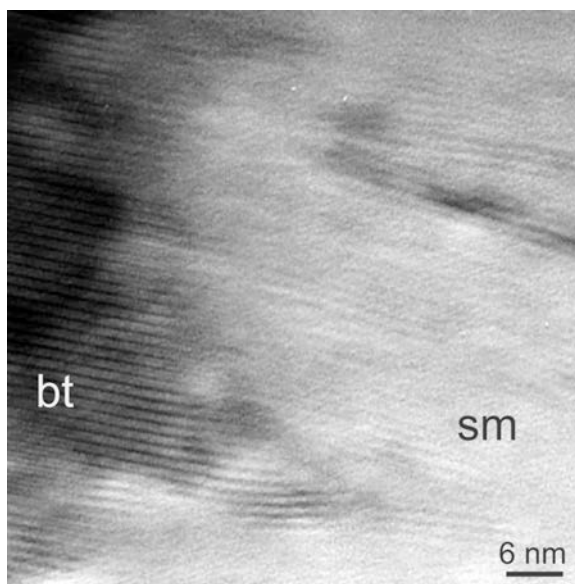
Figure 10. Lattice fringe image of a hydrothermally altered biotite microlite (bt) with regular lattice fringes that have a spacing of 1.0 nm. Along its rim, the biotite crystal is replaced by topotactically oriented smectite (sm) showing irregular lattice fringes.

formula unit (a.p.f.u.). The total number of octahedral cations in these smectite flakes varies from 4.04 to 4.27 a.p.f.u. (Table 2). The compositions of the smectite flakes analyzed plot in the field of montmorillonite in a triangular plot discriminating smectite according to the cation occupancy of the octahedral positions (Figure 11a). The main interlayer cations in the smectite are Na and K, with Na typically being the dominant alkali element. The interlayer Ca content was found to be below the limit of detection in most smectite crystals analyzed.

Smectite occurring in the same textural setting in samples 03RD0-25 and 30RD30-60 generally has a smaller and more variable octahedral Al concentration of 0.57 to 2.98 a.p.f.u. and a larger number of octahedral cations, ranging from 4.37 to 5.54 a.p.f.u. (Table 2). Small (<6 a.p.f.u.) numbers of octahedral cations in trioctahedral smectite may, at least in part, be explained by small-scale intergrowth with dioctahedal smectite

Table 2. Representative AEM analyses of clay minerals that formed by replacement of interstitial glass in the hydrothermally altered trachybasalt samples from Conical Seamount. Compositions are given in atoms per $O_{20}(OH)_4$.

| | —— 03RD0-25 —— | | | | —— 04RD0-50 —— | | | | —— 18RD50-85 —— | | | | —— 30RD30-60 —— | | | |
	1	2	3	4	5	6	7	8	9	10	11	12	13	14	15	16
Si	6.53	7.74	6.73	7.02	7.81	7.42	7.46	7.64	7.41	7.98	7.97	7.90	6.81	6.32	6.66	6.40
^{IV}Al	1.47	0.26	1.27	0.98	0.19	0.58	0.54	0.36	0.59	0.02	0.03	0.10	1.19	1.68	1.34	1.60
^{VI}Al	0.97	2.19	1.07	1.07	2.74	3.21	3.24	2.57	3.38	2.99	3.14	2.86	2.98	0.62	0.88	0.57
Ti	0.22	n.d.	0.4	0.07	n.d.	0.04	0.03	0.06	n.d.	n.d.	n.d.	n.d.	0.04	0.02	0.03	0.04
Mg	3.28	1.81	3.64	3.59	1.19	0.55	0.58	1.05	0.38	0.79	0.72	1.04	0.80	3.24	2.88	2.99
Fe	1.00	0.38	0.76	0.66	0.34	0.27	0.21	0.45	0.29	0.26	0.18	0.26	0.50	1.48	1.46	1.73
Ca	0.19	0.68	0.15	0.12	n.d.	0.15	0.16	0.21	0.04	n.d.	n.d.	n.d.	0.31	0.30	0.27	0.31
Na	0.22	0.24	0.14	0.21	0.36	0.56	0.55	0.31	0.29	0.51	0.44	0.42	0.09	n.d.	.n.d.	n.d.
K	0.76	0.18	0.65	0.53	0.16	0.06	0.07	0.24	0.35	0.06	n.d.	0.06	0.48	0.09	0.15	0.09
ΣVI	5.47	4.38	5.54	5.39	4.27	4.07	4.06	4.13	4.12	4.04	4.04	4.16	4.37	5.41	5.31	5.33
ΣXII	1.17	1.10	0.94	0.89	0.52	0.77	0.78	0.76	0.68	0.57	0.44	0.48	0.88	0.39	0.42	0.40

All Fe is reported as Fe(III)
n.d. = not detected
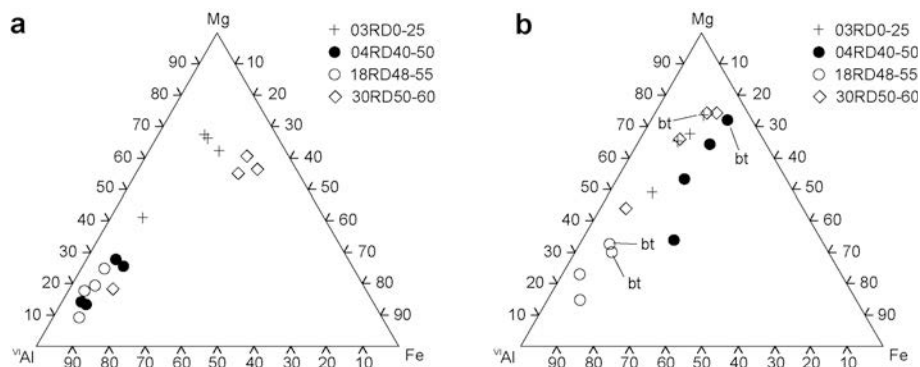ΣVI = sum of octahedral cations
ΣXII = sum of interlayer cations

Figure 11. Triangular plots illustrating the compositional variation of smectite contained in the hydrothermally altered trachybasalt samples. The plots illustrate the relative importance of different cations occupying the octahedral positions in the smectite structure: (a) smectite replacing volcanic glass; (b) smectite replacing pyroxene and biotite (bt; indicated by arrows).

(Figure 12). Smectite flakes having montmorillonite-like and more saponite-like compositions are texturally indistinguishable (Figure 12). Na and K also represent the principal interlayer cations in smectite analyzed in these two samples.

In addition to crystals having montmorillonite-like and saponite-like compositions, rare flakes with compositions approaching high-charge smectite or vermiculite were encountered in the altered glassy groundmass of all four samples. The interlayer cation content of these flakes exceeds 1.1 a.p.f.u., with interlayer charges ranging from 1.3 to 1.5 due to the presence of Ca in the interlayer position (Table 2).
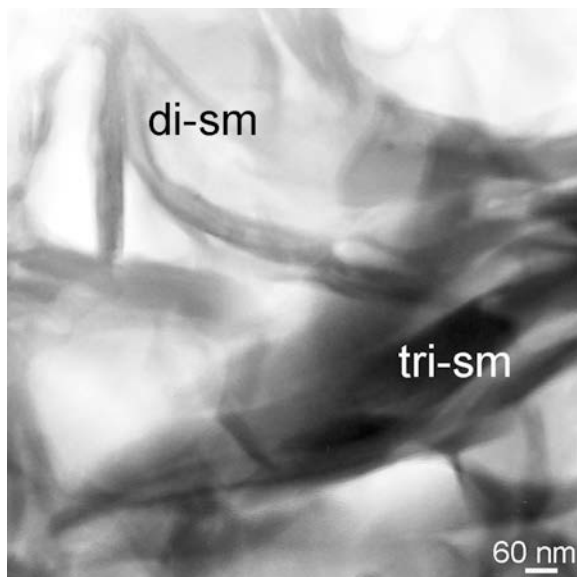

Figure 12. Low-magnification TEM image of the groundmass of hydrothermally altered trachybasalt. Glass alteration resulted in the formation of dioctahedral (di-sm) and trioctahedral (tri-sm) smectite. Flakes of both compositions occur in close association, but form separate crystals.

Smectite crystals replacing pyroxene in the altered trachybasalt samples from Conical Seamount typically show greater Mg concentrations (up to 4.11 a.p.f.u.) and smaller octahedral Al contents (0.46−3.05 a.p.f.u.) than smectite produced by low-temperature devitrification (Table 3). Smectite flakes replacing pyroxene in samples 03RD0-25, 04RD0-50, and 30RD50-60 can be classified as saponite, as they are trioctahedral in nature (Figure 11b) with a positive charge on the octahedral sheet that partially compensates for a large negative charge on the tetrahedral sheet (Table 3). Smectites replacing pyroxene in sample 18RD50-85 show a dioctahedral character, with compositions similar to those of smectites altering glass (Figure 11). Many smectite flakes have K or Na as the dominant interlayer cation, but some flakes show a notable Ca content.

Analysis by AEM of smectite crystals intergrown with biotite, and probably replacing that mineral, revealed that these flakes are usually also typified by comparably large Mg contents and small octahedral Al concentrations, indicating that biotite is typically replaced by saponite. However, some flakes analyzed have relatively large octahedral Al contents warranting classification as montmorillonite (Figure 11). The sum of octahedral cations in these smectite crystals ranges from 4.58 to 5.69 a.p.f.u. (Table 3). In most flakes analyzed, the interlayer position of this trioctahedral smectite is dominated by K.

Chemical analysis of unaltered, interstitial glass also revealed systematic differences between the two groups of trachybasalt samples (Table 4). Volcanic glass contained in the trachybasalt samples 04RD0-50 and 18RD50-85 was found to have relatively large contents of SiO_2 (65.1−67.7 wt.%) and Al_2O_3 (21.7−24.3 wt.%), whereas the concentrations of MgO (4.1−5.4 wt.%) and Fe_2O_3 (1.9−3.2 wt.%) were correspondingly low. The alkali element content of the glass exceeds 1.0 wt.%. Conversely, the glassy matrix of samples 03RD0-25 and 30RD30-60 is typified by distinctly smaller SiO_2 and Al_2O_3 contents (49.6−62.4 wt.% and 14.3−21.4 wt.%,

Table 3. Representative AEM analyses of clay minerals that formed by replacement of pyroxene (analyses 1−3, 5−7, 9, 10, and 13−16) and biotite (analyses 4, 8, 11, and 12) in the hydrothermally altered trachybasalt samples from Conical Seamount. Compositions are given in atoms per $O_{20}(OH)_4$.

| | —— 03RD0-25 —— | | | | —— 04RD0-50 —— | | | | —— 18RD50-85 —— | | | | —— 30RD30-60 —— | | | |
	1	2	3	4	5	6	7	8	9	10	11	12	13	14	15	16
Si	7.01	6.92	7.13	6.77	6.77	7.40	7.12	6.39	7.84	7.77	6.83	6.22	6.95	6.73	6.55	6.97
^{IV}Al	0.99	1.08	0.87	1.23	1.23	0.60	0.88	1.61	0.16	0.23	1.17	1.78	1.05	1.27	1.45	1.03
^{VI}Al	1.95	1.04	1.26	0.71	0.77	1.66	1.34	0.35	3.05	2.99	2.71	2.83	0.46	0.62	2.42	1.24
Ti	n.d.	n.d.	n.d.	0.10	0.19	0.13	0.15	0.24	0.06	0.04	n.d.	n.d.	0.03	n.d.	n.d.	n.d
Mg	2.43	3.63	3.41	4.12	3.19	1.37	2.53	3.64	0.59	0.95	1.50	1.41	4.00	4.11	2.18	3.54
Fe	0.58	0.68	0.56	0.76	0.99	1.03	0.88	1.06	0.35	0.19	0.37	0.48	0.90	0.78	0.35	0.58
Ca	0.10	0.15	0.16	0.17	0.04	0.35	0.06	n.d.	n.d.	0.09	n.d.	0.05	0.43	0.30	0.22	n.d.
Na	0.18	0.36	0.19	0.07	n.d.	n.d.	n.d.	0.11	0.50	0.61	0.30	0.26	n.d.	n.d.	n.d.	0.15
K	0.08	n.d.	n.d.	0.73	0.86	0.80	0.57	1.14	0.07	0.09	0.42	0.49	n.d.	n.d.	0.36	0.20
ΣVI	4.96	5.35	5.23	5.69	5.16	4.22	4.90	5.29	4.05	4.17	4.58	4.80	5.46	5.59	4.99	5.36
ΣXII	0.36	0.51	0.35	0.97	0.90	1.15	0.63	1.25	0.57	0.79	0.72	0.80	0.43	0.30	0.58	0.35

All Fe is reported as Fe(III)
n.d. = not detected
ΣVI = sum of octahedral cations
ΣXII = sum of interlayer cations

respectively), and elevated concentrations of MgO (11.0−15.6 wt.%) and Fe_2O_3 (4.9−14.0 wt.%). The total alkali element content of the glass in these samples is <1.0 wt.%. Analyses by AEM also showed that the CaO content of the volcanic glass in these two samples typically exceeds 1.0 wt.% (Table 4).

DISCUSSION AND CONCLUSIONS

The results of the combined SEM-XRD-TEM-AEM investigation show that hydrothermal alteration of the trachybasalt at Conical Seamount primarily involved a conversion of volcanic glass to smectite. The abundant presence of smectite in the samples investigated constrains the thermal regime of alteration because the mineral is only stable at low temperatures. Research on active geothermal systems has shown that the conversion

of dioctahedral smectite to illite through the formation of mixed-layer illite-smectite is typically initiated at temperatures of ~150ºC (Steiner, 1968; Harvey and Browne, 1991; Inoue et al., 1992; Simmons and Browne, 2000). A similar transformation series occurs for trioctahedral smectite that is converted to mixed-layer chlorite-smectite and chlorite at temperatures exceeding ~200ºC (Kristmannsdottir, 1979; Schiffman and Fridleifsson, 1991; Patrier et al., 1996; Robinson and Santana de Zamora, 1999). As mixed-layered phases or the reaction products of these transformation series have not been observed in the investigated samples, alteration of the trachybasalt is interpreted to have occurred at temperatures below ~150ºC.

Transmission electron microscopy showed that hydrothermally altered glass in the trachybasalt samples from Conical Seamount commonly contains irregularly

Table 4. AEM analyses of unaltered, interstitial volcanic glass contained in trachybasalt from Conical Seamount.

| | 03RD0-25 | | 04RD0-50 | | 18RD50-85 | | 30RD30-60 | |
	1	2	3	4	5	6	7	8
SiO_2	58.67	62.38	65.12	67.57	65.40	67.66	49.57	53.80
TiO_2	n.d.	n.d.	0.93	n.d.	0.38	n.d.	0.37	n.d.
Al_2O_3	21.36	18.27	24.25	21.86	22.99	21.68	14.29	14.51
MgO	12.37	10.97	4.70	5.25	5.38	4.06	15.55	13.90
Fe_2O_3	4.86	6.48	3.21	2.77	1.91	3.18	17.80	13.99
MnO	n.d.	n.d.	n.d.	n.d.	n.d.	n.d.	n.d.	n.d.
CaO	1.26	0.84	n.d.	n.d.	0.67	0.54	2.23	2.79
K_2O	n.d.	0.64	n.d.	n.d.	0.58	0.62	0.57	n.d.
Na_2O	1.00	n.d.	1.39	1.07	2.65	1.97	n.d.	n.d.

The analyses are normalized to 100 wt.%
All Fe is reported as Fe(III)
n.d. = not detected

shaped or elongated domains that are characterized by up to 20 lattice fringes with a spacing of 0.3 to 0.4 nm. These domain structures typically occur in close association with larger smectite flakes. Based on the textural evidence, these short-range ordered domain structures are interpreted to represent transitional alteration products that formed during the glass-to-smectite transition. The poorly crystalline domains appear to have a layer-type structure similar to the primitive clays described by Tazaki *et al.* (1989). However, the structural nature of these phases could not be resolved in the present study because the small size of the domains precluded chemical analysis. At least in some cases, the observed layer spacing of 0.3–0.4 nm could be interpreted to represent a non-basal spacing (Huertas *et al.*, 2004).

Previous research has shown that the formation of transitional alteration products during low-temperature devitrification is not restricted to certain glass compositions. Short-range-ordered, transitional alteration products are common devitrification products of mafic glass (Eggleton and Keller, 1982; Zhou and Fyfe, 1989; Zhou *et al.*, 1992; Stroncik and Schmincke, 2001), but also occur in altered glass of felsic composition (Tazaki *et al.*, 1989; Kawano *et al.*, 1993; Masuda *et al.*, 1996; Fiore *et al.*, 2001). The structural characteristics of these phases are, however, variable, suggesting that different types of metastable alteration products can form during glass alteration. For instance, Tazaki *et al.* (1989) reported the occurrence of short-range ordered, transitional alteration products in experimentally altered volcanic glass that have layer spacings of 0.3–0.33 nm, 0.5 nm, 0.7 nm, 0.8 nm, and 1.0 nm. The presence of such a wide range of layer spacings contrasts with the findings of the present study where only one type of domain structure was observed.

In addition to an indirect reaction series involving the formation of short-range ordered, transitional alteration products, devitrification under low-temperature hydrothermal conditions can also occur through a direct transformation of volcanic glass to smectite (Banfield *et al.*, 1991; Giorgetti *et al.*, 2001, 2006; Zhou *et al.*, 2001). For example, Giorgetti *et al.* (2006) recorded such a direct conversion for dacite recovered from the submarine Pacmanus hydrothermal vent field in the Manus basin, Papua New Guinea. Alteration of glass was found to be most pronounced adjacent to perlitic cracks and vesicles that formed an interconnected network focusing fluid flow. Investigations by HRTEM showed that glass dissolution adjacent to these fluid pathways resulted in a characteristic alteration texture at the nanometer scale. The altered non-crystalline matrix contained abundant round cavities that were partially coated or filled by newly precipitated smectitic flakes. Domain structures similar to those of the present study were not observed in the altered dacite from the Pacmanus hydrothermal vent field.

The available evidence suggests that at least two alteration pathways can occur during the glass-to-smectite transformation in low-temperature hydrothermal environments. Following Peacor (1992), Essene and Peacor (1995), and Robinson *et al.* (2002), the different pathways of glass alteration are interpreted in terms of irreversible, episodic reactions that proceed in one or more steps with a minimization of free energy. Consequently, the glass-to-smectite transition can be viewed as a kinetically controlled reaction progress sequence.

One of the principal kinetic factors influencing reaction pathway and reaction progress of the glass-to-smectite transition appears to be the mode of fluid transport triggering alteration in the low-temperature hydrothermal environment. In the case of the trachybasalt from Conical Seamount, alteration probably proceeded at a comparably low fluid-rock ratio as the low permeability of the coherent rocks and the absence of primary fractures and joints restricted fluid circulation. Under these conditions of limited supply of chemical reactants from the hydrothermal fluids, nucleation of a metastable, poorly crystalline alteration product was kinetically favored permitting a stepwise conversion of glass to smectite. In contrast, high fluid-rock ratios may promote a direct transformation of glass to smectite as chemical reactants supplied by the hydrothermal fluids are readily available at the reactions site. In coherent volcanic rocks, such conditions are probably attained if alteration proceeds along interconnected fluid pathways such as cooling fractures and joints (Marescotti *et al.*, 2000; Giorgetti *et al.*, 2006; Monecke *et al.*, 2007).

The study of the altered trachybasalt from Conical Seamount shows that the different primary phases are variably susceptible to low-temperature hydrothermal alteration. Volcanic glass was found to be most susceptible to alteration under these conditions, followed by pyroxene and biotite. Feldspars are the most resistant primary phases present and no direct indication of alteration has been identified using the applied techniques. Due to different alteration susceptibilities of the constituent phases, alteration of the investigated trachybasalt is heterogeneous at the within-sample scale with pronounced differences occurring between the groundmass and the phenocrysts or microphenocrysts.

The mode by which alteration proceeded within individual phenocrysts, microphenocrysts, and microlites was apparently strongly influenced by the crystallographic and microstructural properties of the respective phases. Successive replacement of primary pyroxene by smectite proceeded from the crystal faces inward, but also preferentially progressed along fractures and cleavage planes, oscillatory growth zones of certain compositions, and contacts between intergrown crystals forming glomerocrysts. In contrast to Eggleton (1975) and Banfield *et al.* (1991), a topotactic relationship between clinopyroxene and smectite was not

observed. Thus, pyroxene alteration is interpreted to have proceeded without structural inheritance. However, a topotactic orientation was observed for biotite and smectite implying that the orientation of common structural blocks was maintained during biotite alteration.

The composition of smectite forming during low-temperature hydrothermal alteration at Conical Seamount is strongly influenced by the composition of the replaced host material. Analysis by AEM revealed that the chemical composition of interstitial glass varies demonstrably between the four samples. Compositional trends observed for smectite mirror these differences. Smectite replacing glass with comparably large SiO_2 and Al_2O_3 contents, but small MgO and Fe_2O_3 concentrations, was found to have a large octahedral Al content, warranting classification as montmorillonite. In contrast, montmorillonite- and saponite-like smectite replace glass that is typified by comparably small SiO_2 and Al_2O_3 contents and elevated MgO and Fe_2O_3 concentrations. In comparison to the products of glass alteration, smectite replacing pyroxene generally has the greatest Mg concentrations and a large number of octahedral cations. The results of the AEM analyses are in agreement with the conclusion above that alteration of the trachybasalt at Conical Seamount occurred under rock-dominated conditions where the composition of the alteration products was primarily controlled by the nature of the replaced host material, not the fluid chemistry.

In all four samples investigated, the interlayer position of smectite forming during glass alteration is dominated by Na and K, with some flakes showing significant relative enrichments in K. This is in agreement with previous findings showing that K is preferentially incorporated into the interlayer position of smectite forming under low-temperature hydrothermal conditions (Monecke *et al.*, 2007). The AEM analysis showed that K is present in the interstitial glass of unaltered trachybasalt from Conical Seamount although this element probably largely resides in sanidine and biotite forming microlites in the groundmass. Unaltered lavas from Conical Seamount are highly potassic containing 2.3 to 3.3 wt.% K_2O, with K_2O/Na_2O ratios ranging from 0.9 to 1.5 (Müller *et al.*, 2003). The hydrothermal fluids interacting with the trachybasalt were probably also enriched in this element, however. The polymetallic veins at Conical Seamount contain abundant secondary monoclinic K-feldspar that presumably directly precipitated from the hydrothermal fluids (Petersen *et al.*, 2002; Monecke *et al.*, 2003).

The results presented provide compelling evidence that the alteration of glassy volcanic rocks in low-temperature hydrothermal environments is not a simple process predictable by equilibrium thermodynamics. Reaction pathway and reaction progress are kinetically controlled and closely related to the mode of fluid transport and the fluid-rock ratio. Alteration is strongly influenced by factors such as the textural characteristics of the volcanic rocks, the presence of interconnected fluid pathways, the mineralogical composition of the rocks, the alteration susceptibility of the constituent phases, and their crystallographic and microstructural properties.

REFERENCES

Alt, J.C. and Teagle, D.A.H. (2003) Hydrothermal alteration of upper oceanic crust formed at a fast-spreading ridge: Mineral, chemical, and isotopic evidence from ODP Site 801. *Chemical Geology*, **201**, 191−211.

Alt, J.C., Honnorez, J., Laverne, C., and Emmermann, R. (1986) Hydrothermal alteration of a 1 km section through the upper oceanic crust, Deep Sea Drilling Project Hole 504B: Mineralogy, chemistry, and evolution of seawater-basalt interactions. *Journal of Geophysical Research*, **91**, 10309−10335.

Alt, J.C., Teagle, D.A.H., Brewer, T., Shanks, W.C. III, and Halliday, A. (1998) Alteration and mineralization of an oceanic forearc and the ophiolite-ocean crust analogy. *Journal of Geophysical Research*, **103**, 12365−12380.

Andrews, A.J. (1980) Saponite and celadonite in layer 2 basalts, DSDP Leg 37. *Contributions to Mineralogy and Petrology*, **73**, 323−340.

Banfield, J.F., Jones, B.F., and Veblen, D.R. (1991) An AEM-TEM study of weathering and diagenesis, Abert Lake, Oregon: I. Weathering reactions in the volcanics. *Geochimica et Cosmochimica Acta*, **55**, 2781−2793.

Bergmann, J., Friedel, P., and Kleeberg, R. (1998) BGMN − A new fundamental parameters based Rietveld program for laboratory X-ray sources, its use in quantitative analysis and structure investigations. *CPD Newsletter*, **20**, 5−8.

Edmond, J.M., Measures, C., McDuff, R.E., Chan, L.H., Collier, R., Grant, B., Gordon, L.I., and Corliss, J.B. (1979) Ridge crest hydrothermal activity and the balances of the major and minor elements in the ocean: The Galapagos data. *Earth and Planetary Science Letters*, **46**, 1−18.

Eggleton, R.A. (1975) Nontronite topotaxial after hedenbergite. *American Mineralogist*, **60**, 1063−1068.

Eggleton, R.A. and Keller, J. (1982) The palagonitization of

limburgite glass − A TEM study. *Neues Jahrbuch für Mineralogie Monatshefte*, **1982**, 321−336.

Essene, E.J. and Peacor, D.R. (1995) Clay mineral thermometry − A critical perspective. *Clays and Clay Minerals*, **43**, 540−553.

Fiore, S., Huertas, F.J., Huertas, F., and Linares, J. (2001) Smectite formation in rhyolitic obsidian as inferred by microscopic (SEM-TEM-AEM) investigation. *Clay Minerals*, **36**, 489−500.

Gemmell, J.B., Sharpe, R., Jonasson, I.R., and Herzig, P.M. (2004) Sulfur isotope evidence for magmatic contributions to submarine and subaerial gold mineralization: Conical Seamount and the Ladolam gold deposit, Papua New Guinea. *Economic Geology*, **99**, 1711−1725.

Giorgetti, G., Marescotti, P., Cabella, R., and Lucchetti, G. (2001) Clay mineral mixtures as alteration products in pillow basalt from the eastern flank of Juan de Fuca Ridge: A TEM-AEM study. *Clay Minerals*, **36**, 75−91.

Giorgetti, G., Monecke, T., Kleeberg, R., and Hannington, M.D. (2006) Low-temperature hydrothermal alteration of silicic glass at the Pacmanus hydrothermal vent field, Manus basin: An XRD, SEM and AEM-TEM study. *Clays and Clay Minerals*, **54**, 240−251.

Harvey, C.C. and Browne, P.R.L. (1991) Mixed-layer clay geothermometry in the Wairakei geothermal field, New Zealand. *Clays and Clay Minerals*, **39**, 614−621.

Herzig, P., Hannington, M., McInnes, B., Stoffers, P., Villinger, H., Seifert, R., Binns, R., and Liebe, T. (1994) Submarine volcanism and hydrothermal venting studied in Papua, New Guinea. *EOS Transactions of the American Geophysical Union*, **75**, 513 and 515−516.

Herzig, P.M., Petersen, S., and Hannington, M.D. (1999) Epithermal-type gold mineralization at Conical Seamount: A shallow submarine volcano south of Lihir Island, Papua New Guinea. Pp. 527−530 in: *Mineral Deposits: Processes to Processing* (C.J. Stanley *et al.*, editors). Balkema, Rotterdam.

Huertas, F.J., Fiore, S., and Linares, J. (2004) In situ transformation of amorphous gels into spherical aggregates of kaolinite: A HRTEM study. *Clay Minerals*, **39**, 423−431.

Humphris, S.E. and Thompson, G. (1978) Hydrothermal alteration of oceanic basalts by seawater. *Geochimica et Cosmochimica Acta*, **42**, 107−125.

Inoue, A., Utada, M., and Wakita, K. (1992) Smectite-to-illite conversion in natural hydrothermal systems. *Applied Clay Science*, **7**, 131−145.

Kadko, D., Baross, J., and Alt, J. (1995) The magnitude and global implications of hydrothermal flux. Pp. 446−466 in: *Seafloor Hydrothermal Systems: Physical, Chemical, Biological and Geological Interactions* (S.E. Humphris, R.A. Zierenberg, L.S. Mullineaux and R.E. Thomson, editors). Geophysical Monograph **91**, American Geophysical Union, Washington.

Kawano, M., Tomita, K., and Kamino, Y. (1993) Formation of clay minerals during low temperature experimental alteration of obsidian. *Clays and Clay Minerals*, **41**, 431−441.

Kristmannsdottir, H. (1979) Alteration of basaltic rocks by hydrothermal activity at 100−300ºC. Pp. 359−367 in: *International Clay Conference 1978* (M.M. Mortland and V.C. Farmer, editors). Developments in Sedimentology, **27**, Elsevier, Amsterdam.

Li, G., Peacor, D.R., and Coombs, D.S. (1997) Transformation of smectite to illite in bentonite and associated sediments from Kaka Point, New Zealand: Contrast in rate and mechanism. *Clays and Clay Minerals*, **45**, 54−67.

Licence, P.S., Terrill, J.E., and Fergusson, L.J. (1987) Epithermal gold mineralisation, Ambitle Island, Papua New Guinea. Pp. 273−278 in: *Pacific Rim Congress 87: An International Congress on the Geology, Structure, Mineralisation and Economics of the Pacific Rim*. The Australasian Institute of Mining and Metallurgy, Parkville, Victoria.

Marescotti, P., Vanko, D.A., and Cabella, R. (2000) From oxidizing to reducing alteration: Mineralogical variations in pillow basalts from the East Flank, Juan de Fuca ridge. Pp. 119−136 in: *Hydrothermal Circulation in the Oceanic Crust: Eastern Flank of the Juan de Fuca Ridge* (A. Fisher, E.E. Davis, and C. Escutia, editors). Proceedings ODP Scientific Results **168**, Ocean Drilling Program, College Station, Texas.

Masuda, H., O'Neil, J.R., Jiang, W.T., and Peacor, D.R. (1996) Relation between interlayer composition of authigenic smectite, mineral assemblages, I/S reaction rate and fluid composition in silicic ash of the Nankai trough. *Clays and Clay Minerals*, **44**, 443−459.

McInnes, B.I.A. and Cameron, E.M. (1994) Carbonated, alkaline hybridizing melts from a sub-arc environment: Mantle wedge samples from the Tabar-Lihir-Tanga-Feni arc, Papua New Guinea. *Earth and Planetary Science Letters*, **122**, 125−141.

Monecke, T., Petersen, S., Herzig, P.M., Petzold, R., and Kleeberg, R. (2003) Shallow submarine gold mineralization at Conical Seamount, Papua New Guinea: Initial results of an alteration halo study. Pp. 155−158 in: *Mineral Exploration and Sustainable Development* (D. Eliopoulos *et al.*, editors). Millpress, Rotterdam.

Monecke, T., Giorgetti, G., Scholtysek, O., Kleeberg, R., Götze, J., Hannington, M.D., and Petersen, S. (2007) Textural and mineralogical changes associated with the incipient hydrothermal alteration of glassy dacite at the submarine PACMANUS hydrothermal system, eastern Manus basin. *Journal of Volcanology and Geothermal Research*, **160**, 23−41.

Mottl, M.J. and Wheat, C.G. (1994) Hydrothermal circulation through mid-ocean ridge flanks: Fluxes of heat and magnesium. *Geochimica et Cosmochimica Acta*, **58**, 2225−2237.

Müller, D., Franz, L., Petersen, S., Herzig, P.M., and Hannington, M.D. (2003) Comparison between magmatic activity and gold mineralization at Conical Seamount and Lihir Island, Papua New Guinea. *Mineralogy and Petrology*, **79**, 259−283.

Patrier, P., Papapanagiotou, P., Beaufort, D., Traineau, H., Bril, H., and Rojas, J. (1996) Role of permeability versus temperature in the distribution of the fine (<0.2 μm) clay fraction in the Chipilapa geothermal system (El Salvador, Central America). *Journal of Volcanology and Geothermal Research*, **72**, 101−120.

Peacock, M.A. (1926) The petrology of Iceland. Part I. The basic tuffs. *Transactions of the Royal Society of Edinburgh*, **55**, 53−76.

Peacor, D.R. (1992) Diagenesis and low-grade metamorphism of shales and slates. Pp. 335−380 in: *Minerals and Reactions at the Atomic Scale: Transmission Electron Microscopy* (P. Buseck, editor). Reviews in Mineralogy, **27**, Mineralogical Society of America, Washington, D.C.

Petersen, S., Herzig, P.M., Hannington, M.D., Jonasson, I.R., and Arribas, A., Jr. (2002) Submarine gold mineralization near Lihir Island, New Ireland fore-arc, Papua New Guinea. *Economic Geology*, **97**, 1795−1813.

Petersen, S., Herzig, P.M., Kuhn, T., Franz, L., Hannington, M.D., Monecke, T., and Gemmell, J.B. (2005) Shallow drilling of seafloor hydrothermal systems using the BGS Rockdrill: Conical Seamount (New Ireland fore-arc) and Pacmanus (eastern Manus basin), Papua New Guinea. *Marine Georesources and Geotechnology*, **23**, 175−193.

Robinson, D. and Santana de Zamora, A. (1999) The smectite to chlorite transition in the Chipilapa geothermal system, El Salvador. *American Mineralogist*, **84**, 607−619.

Robinson, D., Schmidt, S.T., and Santana de Zamora, A. (2002) Reaction pathways and reaction progress for the smectite-to-chlorite transformation: Evidence from hydrothermally altered metabasites. *Journal of metamorphic Geology*, **20**, 167−174.

Rytuba, J.J., McKee, E.H., and Cox, D.P. (1993) Geochronology and geochemistry of the Ladolam gold deposit, Lihir Island, and gold deposits and volcanoes of Tabar and Tatau, Papua New Guinea. *U.S. Geological Survey Bulletin*, **2039**, 119−126.

Schiffman, P. and Fridleifsson, G.O. (1991) The smectite-chlorite transition in drillhole NJ-15, Nesjavellir geothermal field, Iceland: XRD, BSE and electron microprobe investigations. *Journal of Metamorphic Geology*, **9**, 679−696.

Shau, Y.H. and Peacor, D.R. (1992) Phyllosilicates in hydrothermally altered basalts from DSDP Hole 504B, Leg 83 − A TEM and AEM study. *Contributions to Mineralogy and Petrology*, **112**, 119−133.

Simmons, S.F. and Browne, P.R.L. (2000) Hydrothermal minerals and precious metals in the Broadlands-Ohaaki geothermal system: Implications for understanding low-sulfidation epithermal environments. *Economic Geology*, **95**, 971−999.

Spivack, A.J. and Staudigel, H. (1994) Low-temperature alteration of the upper oceanic crust and the alkalinity budget of seawater. *Chemical Geology*, **115**, 239−247.

Staudigel, H. and Hart, S.R. (1983) Alteration of basaltic glass: Mechanisms and significance for the oceanic crust-seawater budget. *Geochimica et Cosmochimica Acta*, **47**, 337−350.

Steiner, A. (1968) Clay minerals in hydrothermally altered rocks at Wairakei, New Zealand. *Clays and Clay Minerals*, **16**, 193−213.

Stewart, W.D. and Sandy, M.J. (1988) Geology of New Ireland and Djaul Islands, northeastern Papua New Guinea. Pp. 13−30 in: *Geology and Offshore Resources of Pacific Island Arcs − New Ireland and Manus Region, Papua New Guinea* (M.S. Marlow, S.V. Dadisman and N.F. Exon, editors). Earth Science Series **9**, Circum-Pacific Council for Energy and Mineral Resources, Houston, Texas.

Stroncik, N.A. and Schmincke, H.U. (2001) Evolution of palagonite: Crystallization, chemical changes, and element budget. *Geochemistry Geophysics Geosystems*, **2**, 2000GC000102.

Tazaki, K., Fyfe, W.S., and van der Gaast, S.J. (1989) Growth of clay minerals in natural and synthetic glasses. *Clays and Clay Minerals*, **37**, 348−354.

Ufer, K., Roth, G., Kleeberg, R., Stanjek, H., Dohrmann, R., and Bergmann, J. (2004) Description of X-ray powder pattern of turbostratically disordered layer structures with a Rietveld compatible approach. *Zeitschrift für Kristallographie*, **219**, 519−527.

Ufer, K., Stanjek, H., Roth, G., Dohrmann, R., Kleeberg, R., and Kaufhold, S. (2008) Quantitative phase analysis of bentonites by the Rietveld method. *Clays and Clay Minerals*, **56**, 272−282.

Zhou, Z. and Fyfe, W.S. (1989) Palagonitization of basaltic glass from DSDP Site 335, Leg 37: Textures, chemical composition, and mechanism of formation. *American Mineralogist*, **74**, 1045−1053.

Zhou, Z., Fyfe, W.S., Tazaki, K., and van der Gaast, S.J. (1992) The structural characteristics of palagonite from DSDP Site 335. *The Canadian Mineralogist*, **30**, 75−81.

Zhou, W., Peacor, D.R., Alt, J.C., van der Voo, R., and Kao, L.S. (2001) TEM study of the alteration of interstitial glass in MORB by inorganic processes. *Chemical Geology*, **174**, 365−376.